



Power Electronic Systems
Laboratory

© 2016 IEEE

IEEE Transactions on Industry Applications, Vol. 52, No. 1, pp. 172-180, January/February 2016

Evaluation of One- and Two-Pole-Pair Slotless Bearingless Motors With Toroidal Windings

D. Steinert
T. Nussbaumer
J. W. Kolar

This material is published in order to provide access to research results of the Power Electronic Systems Laboratory / D-ITET / ETH Zurich. Internal or personal use of this material is permitted. However, permission to reprint/republish this material for advertising or promotional purposes or for creating new collective works for resale or redistribution must be obtained from the copyright holder. By choosing to view this document, you agree to all provisions of the copyright laws protecting it.



Eidgenössische Technische Hochschule Zürich
Swiss Federal Institute of Technology Zurich

Evaluation of One- and Two-Pole-Pair Slotless Bearingless Motors With Toroidal Windings

Daniel Steinert, *Student Member, IEEE*, Thomas Nussbaumer, *Member, IEEE*, and Johann W. Kolar, *Fellow, IEEE*

Abstract—In this paper, winding topologies for one- and two-pole-pair rotors are analyzed and compared for a slotless bearingless disk drive with toroidal windings. The basis of the studies is a six-phase motor with a diametrically magnetized one-pole-pair rotor. Due to the absence of mechanical bearings and the significantly large air-gap capability, the motor is suitable for applications with high purity and special chemical demands. Its slotless design results in low losses even at high rotational speeds. To improve the operational behavior of the rotor in different applications, the influence of higher pole pair numbers on the passive bearing stiffness is examined. A possible winding configuration for these rotors is proposed and evaluated for their bearing and motor performance. Based on the results, a further prototype was built and is presented in this paper.

Index Terms—Active magnetic bearing, bearingless motor, high-speed drive, slotless motor.

I. INTRODUCTION

IN a bearingless permanent-magnet (PM) synchronous motor, the rotor is spatially suspended and rotated without any mechanical contact [1]. Due to the lack of lubrication and abrasion, as well as the possibility to hermetically isolate the rotor and stator from the environment, bearingless motors and magnetically suspended motors are used, for example, in semiconductor manufacturing [2], in pumps or mixers for delicate fluids [3]–[7], or in high-speed applications [8], [9].

Due to the absence of mechanical contact between the rotor and stator, mechanical bearings and shaft feedthroughs can be omitted. This allows for a hermetic encapsulation of the rotor and stator, which results in high resistance against chemically aggressive fluids and gases and in increased lifetime compared with conventional motors. The absence of abrasion and lubrication enables operation in high-purity applications.

In the presented slotless bearingless motor concepts, a ring-shaped rotor is magnetically levitated without mechanical contact in the middle of an annular stator. This disk topology results

Manuscript received June 30, 2014; revised November 30, 2014, February 27, 2015, and June 4, 2015; accepted July 30, 2015. Date of publication August 11, 2015; date of current version January 18, 2016. Paper 2014-EMC-0523.R3, presented at the 2014 International Power Electronics Conference (IPEC-Hiroshima 2014 ECCE-Asia), Hiroshima, Japan, May 18–21, and approved for publication in the IEEE TRANSACTIONS ON INDUSTRY APPLICATIONS by the Electric Machines Committee of the IEEE Industry Applications Society.

D. Steinert and J. W. Kolar are with the Power Electronic Systems Laboratory, Swiss Federal Institute of Technology Zurich (ETH Zurich), 8092 Zurich, Switzerland (e-mail: steinert@lem.ee.ethz.ch; kolar@lem.ee.ethz.ch).

T. Nussbaumer is with Levitronix GmbH, 8005 Zurich, Switzerland (e-mail: nussbaumer@levitronix.com).

Color versions of one or more of the figures in this paper are available online at <http://ieeexplore.ieee.org>.

Digital Object Identifier 10.1109/TIA.2015.2466683

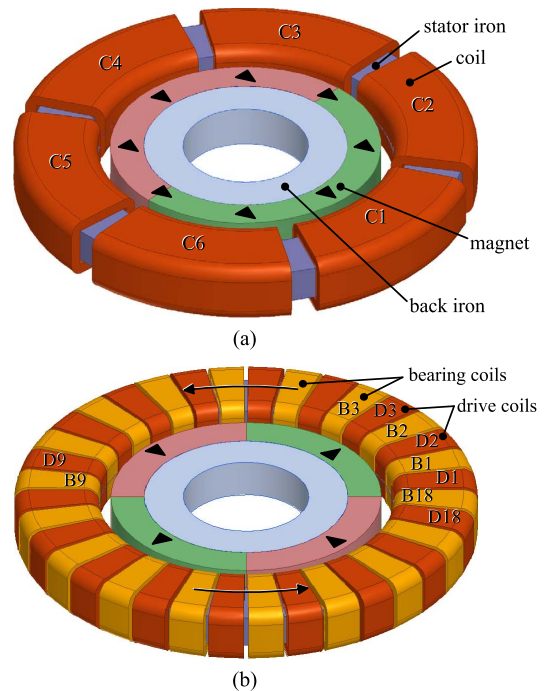


Fig. 1. Principle setup of two different slotless bearingless disk drives. Novel topology B features a two-pole-pair rotor and therefore has improved passive bearing stiffness. Topology A has combined coils and generates force and torque simultaneously with the same set of coils as a sum of motor and suspension currents will be supplied. (a) Topology A. (b) Topology B.

in enhanced compactness due to its low axial length. The coils, which are toroidally wound on the stator iron, can generate both bearing forces and drive torque. This slotless motor topology has the advantage of reduced losses at high rotational and circumferential speeds compared with conventional slotted machines.

Especially when big air gaps are required, for example, due to a chemical sealing, bearingless motors have significantly lower bearing stiffness than mechanical ones, which limits possible applications. In pumps and blowers, for instance, axial and radial forces resulting from the differential pressure of the fluid act on the impeller. This means a considerable movement of the magnetically levitated rotor and limits the achievable pump, blower, or turbine performance [10].

Motors with a one-pole-pair diametrical magnetized rotor and six or ten coils are already proposed in [11]–[13]. To improve both the passive bearing stiffness and the active bearing and motor performance of the bearingless motor, different rotor magnetizations, rotor pole pair numbers, and winding configurations are necessary. Fig. 1 shows the two topologies that are evaluated. The coils are enumerated to show the connection

of the coils in the schematics, which will be shown later. Topology A has six coils and a one-pole-pair diametrical rotor, as presented by the authors in [11]. This is the best topology when low losses are demanded. Novel topology B uses a two-pole-pair rotor and therefore features higher passive stiffness values, which can be important, for example, in blower or pumping applications. The two topologies will be analyzed and compared in this paper.

It has to be distinguished between combined coils, where drive and bearing currents are superposed on one set of coils, and separate coils for motor and bearing. In [14] and [15], a slotted bearingless motor with combined windings is presented, and it is shown that combined windings lead to a more compact and simple winding scheme. However, with 3 three-phase inverters, the power electronics are quite extensive.

The goal is now to find a possible winding scheme with low complexity in winding and power electronics for rotors with two-pole pairs. We will show that, with a two-pole-pair rotor, the passive bearing stiffness is significantly increased.

At first, the magnetic air-gap field distributions of rotors with different pole pair numbers are evaluated. The influence of the pole pair number on the passive bearing stiffness values is shown.

As only specific winding configurations are capable of generating torque and force independently for given rotor magnetization, we derive the criteria for developing suitable configurations for separated and combined winding schemes. The winding concepts differ with regard to the coil number and the interconnection of the coils.

By 3-D finite-element (FE) simulations, the selected winding topologies are compared regarding their bearing and motor capabilities, as well as passive stiffness values. Additionally, possible loss mechanisms and the influence of the pole pair number onto the losses are discussed. At the end, a prototype of topology B with a two-pole-pair rotor will be presented and compared with the prototype of topology A. It will be shown that novel topology B is preferable in applications, where high bearing stiffness values are necessary. However, lower losses at high speeds can be achieved with topology A.

II. WORKING PRINCIPLE OF THE SLOTLESS BEARINGLESS DISK DRIVE

In [11], the authors present the detailed working principles and simulation and test results of the bearingless slotless disk drive with six coils and a diametrically magnetized one-pole-pair rotor. The presented prototype is the basis for the topology evaluation in this paper.

A. Passive Bearing Stiffness Values

The disk-type bearingless motor is passively stable in the tilting and axial directions and has to be actively controlled in the radial direction. Fig. 2 shows the magnetic field that is generated by the PMs on the rotor for a one-pole-pair (P1) and a two-pole-pair (P2) magnetization. For the P1 magnetization, the axes of magnetization (d -axis) and the orthogonal direction (q -axis) are highlighted. This magnetic field generates reluctance forces between the stator iron and the rotor. Therefore,

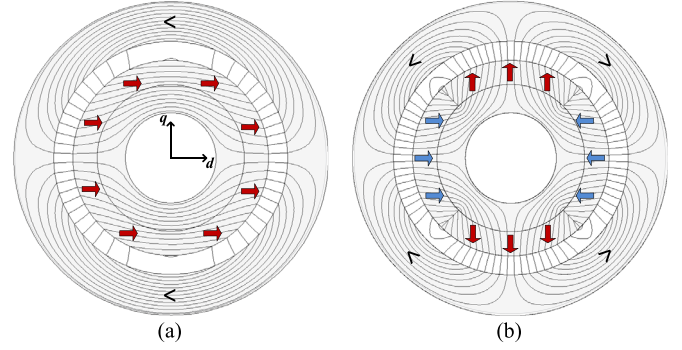


Fig. 2. Simulated flux plots with only rotor PM with no currents. A diametrically magnetized one-pole-pair rotor (rotor P1) and a two-pole-pair rotor (rotor P2) are shown. (a) Rotor P1. (b) Rotor P2.

deflection in the axial z -direction will lead to a counteracting force

$$dF_z = -c_z \cdot dz \quad (1)$$

due to the axial stiffness constant c_z similar to a spring constant. With this definition, a positive value of the stiffness leads to a stabilizing force.

Similarly, tilting of the rotor results in a counteracting torque. At a rotor with P1 magnetization, it has to be distinguished between the rotation around the axis of magnetization (angle α) and the rotation perpendicular to it (angle β). The tilting stiffness values c_α and c_β are then defined as

$$c_\alpha = -\frac{dT_\alpha}{d\alpha} \text{ and } c_\beta = -\frac{dT_\beta}{d\beta}. \quad (2)$$

When the rotor is displaced from its center position in the radial direction, a radial force will act in the same direction. Therefore, the radial stiffness values

$$c_d = -\frac{dF_x}{dx_d} \text{ and } c_q = -\frac{dF_y}{dx_q} \quad (3)$$

are destabilizing. Here, x_d means a displacement in the direction of the magnetization and x_q means a displacement perpendicular to the magnetization.

A one-pole-pair rotor results in anisotropic radial and tilting stiffness. Deflection of the rotor in the direction of magnetization (d -axis) results in a higher attractive force than deflection perpendicular to the magnetization (q -axis). The same holds for the tilting stiffness. Rotation around the d -axis results in a lower torque than rotation around the q -axis. This results in a broad resonance frequency range, as shown in [16]. Rotors with higher pole pair numbers, however, show almost isotropic stiffness values in all directions

$$\begin{aligned} P = 1 : c_\alpha < c_\beta \text{ and } c_q < c_d \\ P \geq 2 : c_\alpha \approx c_\beta \text{ and } c_q \approx c_d. \end{aligned} \quad (4)$$

Therefore, rotor magnetizations of two or more pole pairs are favorable for increased bearing stability.

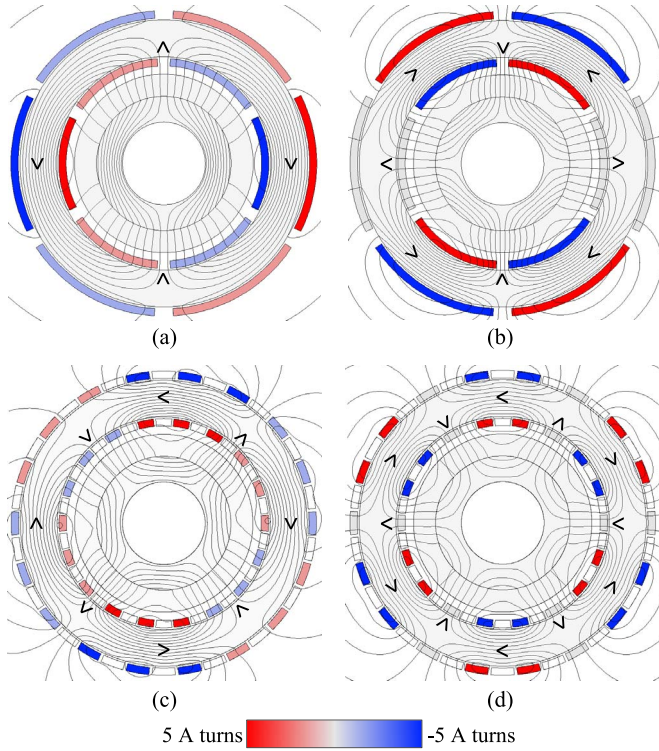


Fig. 3. Simulated armature reaction field due to the coil currents indicated by different shades of blue and red. Depending on the type of the current, each topology generates the corresponding field for force or torque generation. The rotor is not magnetized in this simulation to only show the armature field. (a) Topology A-P1 with drive current. (b) Topology A-P1 with bearing current. (c) Topology B with drive current. (d) Topology B with bearing current.

B. Bearing Force and Drive Torque Generation

The stator of the bearingless motor has to produce both suspension force and drive torque simultaneously. For a resulting torque acting on the rotor, the stator coils have to generate a magnetic armature reaction field in the magnetic gap with a pole pair number

$$p_{\text{drv}} = p \quad (5)$$

which is equal to the pole pair number p of the rotor magnetic field. A force will be generated by a stator field with a pole pair number

$$p_{\text{bng}} = p \pm 1 \quad (6)$$

as described in [17].

Fig. 2 shows the simulated flux plots of rotors P1 and P2 with no currents in the coils. Fig. 3 shows the simulated armature reaction field of topologies A and B. The rotor is not magnetized in this simulation to only show the stator field. It shows that, depending on the current scheme, topology A produces a one-pole-pair field with a drive current [see Fig. 3(a)] and a two-pole-pair field with a bearing current [see Fig. 3(b)]. This correlates to the one-pole-pair rotor field. Respectively, topology B generates a $p_{\text{drv}} = 2$ field for the drive and a $p_{\text{bng}} = 3$ field for the bearing corresponding to the two-pole-pair rotor.

In Fig. 4, the superposition of the PM rotor field and armature reaction field resulting from a bearing current is exemplarily

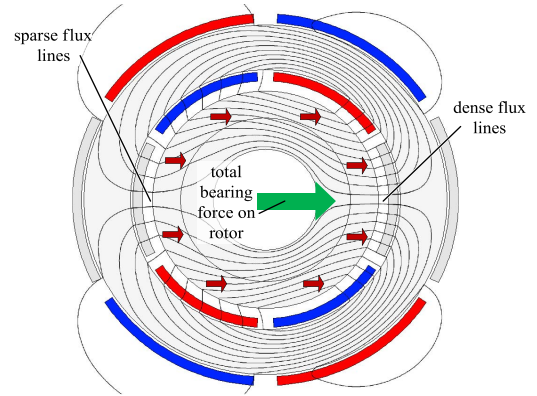


Fig. 4. Superposition of the magnetic field of the rotor (rotor P1) and a two-pole-pair armature reaction field resulting from a bearing current in topology A. Lorentz and reluctance forces add up to the total bearing force acting on the rotor.

shown for topology A. This corresponds to a combination of Fig. 2(a) with Fig. 3(b). In this case, the armature reaction field is superposed with the rotor field so that the field density is increased at the right side of the rotor and decreased at the left side. This leads to a force on the rotor toward the stronger field density on the right. Additionally, Lorentz forces are generated by the rotor magnetic field that penetrates the coils in the air gap. The current in the coils generates a force in the tangential direction. Summing up all Lorentz forces in the coils leads to a bearing force in the same direction as the reluctance force. Together, Lorentz and reluctance forces add up to the total bearing force. As shown in [11], the contribution of both force components is approximately equal for the case at hand.

However, this is only true if $p_{\text{bng}} = p + 1$. For an armature reaction field with a pole pair number smaller than that of the rotor ($p_{\text{bng}} = p - 1$), both forces point to opposite directions and partially cancel each other out, as proven in [2]. This would lead to reduced bearing forces, as will be also shown in the 3-D simulation results in Section IV. Therefore, to achieve high bearing forces, a magnetic air-gap field with $p_{\text{bng}} = p + 1$ has to be generated by the set of coils.

By analytic calculation, it can be shown that the bearing force F_{bng} and the drive torque T

$$\vec{F}_{\text{bng}} = k_F \cdot \hat{I}_B \begin{pmatrix} \cos(\varphi_F) \vec{e}_x \\ \sin(\varphi_F) \vec{e}_y \end{pmatrix} \quad (7)$$

$$T = k_T \cdot \hat{I}_D \quad (8)$$

are proportional to the amplitude of bearing current \hat{I}_B or drive current \hat{I}_D [11]. The force coefficient k_F and the drive coefficient k_T can be determined by a finite-element method (FEM) simulation. The force direction can be controlled by the phase shift φ_F between electrical rotor angle and bearing current.

III. EVALUATION OF PASSIVE BEARING PROPERTIES FOR DIFFERENT MAGNET CONFIGURATIONS

Depending on the application, considerably large magnetic gaps are necessary, for instance, if a chemically resistant wall

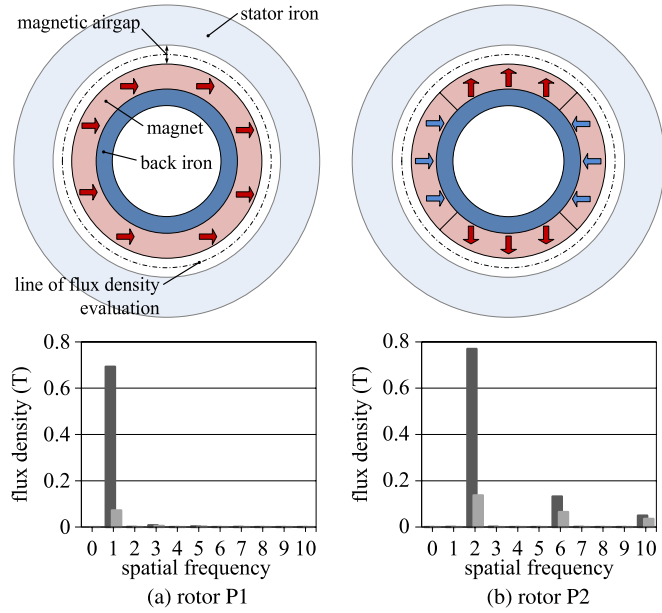


Fig. 5. Schematic of the evaluated magnet configurations (top) for (a) a diametrical one-pole-pair rotor and (b) a two-pole-pair rotor. At the dotted line in the air gap between PM and stator iron, the flux density distribution is analyzed by fast Fourier transform. The resulting tangential and radial field components are shown at the bottom.

has to be inserted between the rotor and stator. This drastically reduces the passive stiffness values of the bearing, as shown in [12]. Therefore, a strong magnetic field in the air gap between magnet and stator iron is important. Moreover, the active force and torque generation depends particularly on the fundamental wave of the flux density distribution in the air gap.

To compare the different magnetizations, a fixed geometry, which was already used in [11], is chosen. The dimensions of stator and magnet, which are the most important dimensions for the evaluation, are shown in Table II (prototype A). This geometry results from an optimization with a one-pole-pair rotor and yields a significantly large air gap, suitable for pump and blower applications.

Fig. 5 shows a diametrical one-pole-pair (P1) and a two-pole-pair (P2) magnet configuration, as well as the harmonic analysis of the magnetic field distribution in the middle of the magnetic gap, which was simulated with a FEM simulation. The diagram below shows that the diametrical magnetization yields a purely sinusoidal magnetic air-gap field. This is the best for a good bearing and drive performance, as well as for lowest losses, as higher harmonics do not contribute to force and torque but generate losses. However, as previously shown, the stiffness values of rotor P1 are anisotropic, which makes it necessary to evaluate higher pole pairs.

For higher pole pair numbers, the magnetization [see Fig. 5(b)] consists of alternately inward and outward magnetized magnets. It yields a higher flux density but also higher harmonics in the field distribution.

The axial stiffness values, which are simulated with a 3-D magnetostatic FEM simulation tool, are shown for different pole pair numbers and magnet configurations in Fig. 6(a). From rotor P1 to rotor P2, the axial stiffness increases by 39%.

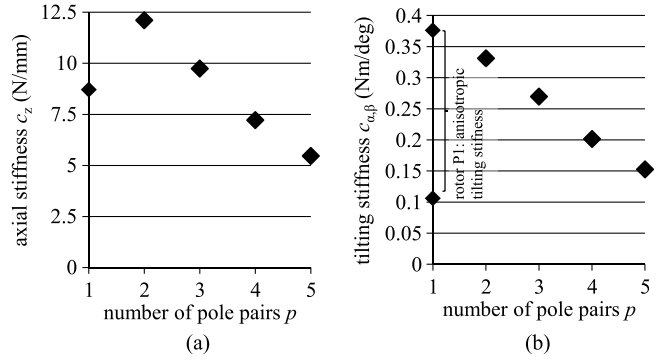


Fig. 6. (a) Axial stiffness and (b) tilting stiffness simulated with a 3-D FEM. As the tilting stiffness of the one-pole-pair rotor depends on the direction of tilting, the highest and lowest tilting stiffness values are indicated.

With pole pair numbers higher than $p = 2$, the stiffness would decrease again.

Similar results are found for the tilting stiffness, which are shown in Fig. 6(b). The tilting stiffness increases by 37% with a two-pole-pair magnetization (P2) compared with the mean tilting stiffness of the one-pole-pair rotor (P1). In Fig. 6(b), the minimum and maximum tilting stiffness are also shown for rotor P1 that results from the aforementioned anisotropy. As the tilting stiffness values are isotropic for the $p \geq 2$ magnetizations, rotor P2 has an increased tilting stiffness value of 300% compared with the minimal value of rotor P1.

Summarizing, the highest passive bearing stiffness values can be achieved with a two-pole-pair rotor. A further increase in the pole number reduces the stiffness values.

IV. WINDING CONCEPTS

For each pole pair number, it is necessary to derive a winding configuration that is capable of generating both torque and force independently.

A. Winding Criteria for Combined Coils

With combined coils, both torque and force are generated by the same set of coils. Because of the different pole numbers for bearing and drive, the winding scheme contains no repetitive elements. This means that the number of phases m is equal to the number of coils N . However, one coil can be separated in two coils with reversed winding direction, which are connected in series, as proposed in [16]. This will have no direct effect on the feasibility of the winding configuration and is not examined in this paper.

To generate a field with a given pole pair number p , the number of coils

$$N \geq 2 \cdot p \quad (9)$$

has to be at least twice as high to avoid aliasing. For the bearing, this is even stricter as there are two degrees of freedom that have to be actively controlled. If the number of poles and coils would be equal, the bearing phases would have a phase shift of

180° and therefore only one degree of freedom. Altogether, the number of coils for the bearing

$$N > 2 \cdot p_{\text{bng}} \tag{10}$$

has to be more than twice as high as the number of pole pairs needed for bearing operation.

For a one-pole-pair rotor, a bearing field with $p = 2$ has to be generated. This leads to a minimal coil number of five. As aforementioned, five- and six-phase motors with a one-pole-pair rotor already exist [11]–[13]. The six-coil topology is referred to as “topology A” in this paper.

Theoretically, this topology is also possible with a two-pole-pair rotor as it can generate a $p_{\text{drv}} = 2$ stator field for the drive and a $p_{\text{bng}} = 1$ ($p_{\text{bng}} = p - 1$) field for the bearing. As aforementioned, this will lead to a low bearing performance. This topology is referred to as “topology A-P2” and will be tested for comparing the losses of one- and two-pole-pair machines, but due to the poor bearing performance, it is not recommendable for any application.

Therefore, with a two-pole-pair rotor, a bearing field with $p_{\text{bng}} = 3$ has to be generated by the coils. A six-coil motor is not able to generate a continuous $p_{\text{bng}} = 3$ stator field as the phases would have a 180° phase shift. With the criteria in (10), at least seven coils are needed for a two-pole-pair rotor. A topology with eight combined coils, which results in less complicated power electronics than with seven coils, is presented by the authors in [18]. As this topology is still quite complicated regarding power electronics and wiring, it will not be discussed here.

B. Winding Criteria for Separated Coils

With separated coils, the magnetic field for each bearing and motor operation is generated by an independent set of coils. Therefore, two independent inverters can be used. Then, the winding configuration consists of repetitive elements corresponding to the respective pole pair number of bearing and motor field.

For the bearing field, at least two phases per pole pair are necessary, as two degrees of freedom have to be controlled. To maintain manufacturability, the coil numbers for bearing and motor should be the same. Therefore, winding configurations with 9, 12, or 18 coils each for bearing and motor are possible.

Simulations of the 2×9 -coil topology showed that, due to adverse field harmonics of the armature reaction field, a coupling of the bearing and the drive system exists. Therefore, this topology will not be explained here, but it is shown in [18]. The 2×12 -coil topology has three phases for the drive and two phases for the bearing. This results in a higher power electronic effort than a solely three-phase system.

The 2×18 -coil topology does not show this disadvantageous behavior and has a three-phase system each for drive and bearing. It is referred to as “topology B” and will be further examined in this paper.

C. Winding Connection

In Fig. 7, the winding connection of the aforementioned motor topologies is shown. The numbering of the coils is shown in Fig. 1. Every coil is wound in the same direction. A negative

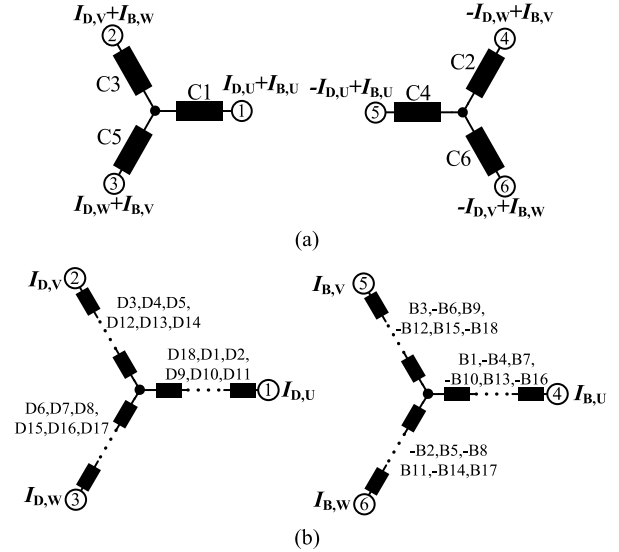


Fig. 7. Winding connection for both topologies. Each motor has two separate star systems with three phases each. In the combined coils of topology A, drive currents $I_{D,U..W}$ and bearing currents $I_{B,U..W}$ are superposed on each phase. For topology A-P2, bearing and drive current have to be swapped. With the separate coils of topology B, there is one designated star system each for bearing and drive. Every coil is wound in the same direction. A negative sign in the winding scheme indicates that the coil connection is reversed. (a) Topology A-P1. (b) Topology B.

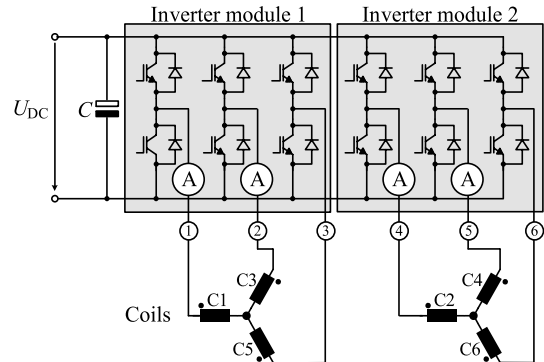


Fig. 8. Schematic circuit of the power electronics suitable all evaluated topologies. The winding connection is exemplarily shown for topology A.

sign in the winding scheme indicates that the coil connection is reversed.

For each topology, we define two independent sets of currents. With the drive currents $I_{D,U}$, $I_{D,V}$, and $I_{D,W}$, the drive torque is generated, whereas the bearing currents $I_{B,U}$, $I_{B,V}$, and $I_{B,W}$ generate the bearing force. Each current system consists of three 120° phase-shifted currents.

As in combined windings the coils generate both force and torque, the drive and bearing currents have to be superposed on the coils. This will lead again to two different separated current systems, as shown in Fig. 7.

For the separate winding concept, the drive currents are directly fed into the three-phase system of the drive coils and similarly with the bearing currents.

The connection of the coils to the power electronics is shown in Fig. 8. The power electronics consist of two inverter modules with six switches each to power 2 three-phase systems.

TABLE I
COMPARISON OF PROPOSED TOPOLOGIES

topology	rotor	k_T $\left(\frac{\text{Nm}}{\text{A/mm}^2}\right)$	k_F $\left(\frac{\text{N}}{\text{A/mm}^2}\right)$	c_z $\left(\frac{\text{N}}{\text{mm}}\right)$	c_α $\left(\frac{\text{Nm}}{\text{deg}}\right)$	c_r $\left(\frac{\text{N}}{\text{mm}}\right)$
A	P1	0.27	4.9	8.7	0.11...0.38	-10...-18
A	P2	0.30	3.9	12.1	0.33	-26
B	P2	0.29	6.6	12.1	0.33	-26

k_T ... torque per peak current density in the coils¹

k_F ... force per peak current density in the coils¹

c_z ... axial stiffness

c_α ... tilting stiffness

c_r ... radial stiffness

¹ assuming a fill factor of 1 in the coil

In Fig. 8, the connection to topology A-P1 is exemplarily shown. For topology A-P2, bearing and drive currents have to be swapped. The connection to topology B is indicated by the numbered connector terminals, which correspond to the terminals in Fig. 7.

D. Simulation Results of the Proposed Topologies

Subsequently, the two topologies have been simulated in 3-D FE simulations. The results are shown in Table I. For comparison reasons, the bearing and drive constants are calculated, assuming a fill factor of 1 in the coils.

It shows that the two-pole-pair rotor has significantly higher passive stiffness values. As expected, the active bearing force of topology A-P2 is significantly lower. Together with the higher destabilizing radial stiffness, the magnetic bearing performance of topology A-P2 is not recommended for real applications.

However, with topology B, the highest bearing force is achievable, which is sufficient to compensate also the high radial stiffness of the two-pole-pair rotor.

Therefore, with novel two-pole-pair topology B, a promising alternative to one-pole-pair topology A-P1 is developed. The passive stiffness values and the active bearing and drive performances exceed the values of topology A-P1.

V. TEST RESULTS

A. Prototypes

For all proposed topologies, two prototypes were built and tested. Prototype A refers to topology A and can be operated with a P1 and a P2 rotor. This allows direct comparison of stiffness and losses for both rotor types. Since prototype A-P2 shows, as expected, very weak bearing performance, a further prototype B with topology B was built.

Prototype ‘‘A-P1’’ with a diametrical magnetized one-pole-pair rotor and six combined coils has been already built and successfully tested [11]. Fig. 9 shows the prototype mounted on a plate together with a printed circuit board for sensor signal amplification. Stable operation is possible for up to 20 000 r/min, which is the mechanical limit of the rotor.

When operating this motor with a two-pole-pair rotor (prototype A-P2), the startup bearing current needed to start the levitation is around 2.7 times higher than with the P1 rotor. During operation, the rotor has to stay perfectly in the radial



Fig. 9. Picture of prototype A with six coils and diametrically magnetized rotor. The annular rotor has an outer diameter of 102 mm and a total height of 18 mm.



Fig. 10. Picture of prototype B with 36 coils and a two-pole-pair radial magnetized rotor. The rotor has an outer diameter of 165 mm and a height of 24 mm.

TABLE II
GEOMETRIC DETAILS OF BOTH PROTOTYPES

	prototype A	prototype B	
rotor configuration	P1, P2	P2	
maximum speed	20 000	12 000	(r/min)
rotor diameter	102	164.8	(mm)
magnet thickness	12	10.2	(mm)
magnet height	15	20	(mm)
back iron thickness	12	8	(mm)
stator inner diameter	116	181.8	(mm)
stator outer diameter	156	221.8	(mm)
stator height	12.5	14	(mm)
stator mass	0.81	1.35	(kg)
magnetic air gap	9.5	11	(mm)

center so that the bearing does not have to generate high forces to compensate for the position offset. Then, stable operation was possible for up to 17 000 r/min.

Additionally, a second prototype (‘‘prototype B’’) with a two-pole-pair rotor and 2×18 separated coils corresponding to topology B is built and depicted in Fig. 10. As higher losses occur with two-pole-pair rotors at the same rotational speed, prototype B was built with a significantly bigger rotor outer diameter so that higher circumferential speeds can be achieved with lower rotational speeds.

While prototype A has a rotor diameter of 102 mm, prototype B has a rotor size of 164.8 mm. The bigger size also enhances the manufacturability, particularly with the high number of coils that have to be placed on the stator of prototype B. The geometrical details of both prototypes are compared in Table II.

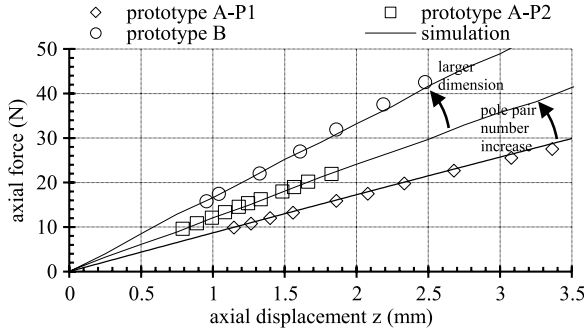


Fig. 11. Axial displacement versus axial force (symbols) measured and (lines) simulated for prototypes A and B.

With prototype B, rotational speeds of up to 12 000 r/min are reached. This is the limit of mechanically safe operation. The prototype showed stable bearing behavior in standstill and during rotation. Rigid body resonances were observed only between 1500 and 2000 r/min, whereas prototype A-P1 is unstable in the range of 500–2000 r/min. This can be explained with the anisotropic radial and tilting stiffness values of prototype A-P1. When the rotor is radially displaced or tilted, the attractive force or torque toward the stator will vary during rotation if the stiffness is not isotropic. This can easily trigger oscillations. Additionally, the different stiffness values of the d - and the q -axes results in a range of resonances with different oscillation modes.

Outside of this range, no resonances occurred. The separation of bearing and drive coils proved to be advantageous during implementation of prototype B as the control of both three-phase current systems is independent. Additionally, the coils for bearing and drive could be adapted in size and number of turns to their respective function.

B. Stiffness Measurements

To confirm that, with the two-pole-pair concepts, significantly higher passive bearing stiffness values can be achieved, the axial stiffness was measured. The axial displacement of the levitated rotor was measured with a laser sensor, whereas the rotor was loaded with different weights. Together with the weight of the rotor, the total axial force could be calculated.

With prototype A, the axial stiffness of the rotor concepts P1 and P2 can be directly compared at the same geometry. The results are shown in Fig. 11. It shows the axial force, calculated by the applied weight, in dependence on the rotor displacement. Additionally, the simulated force, which was used to calculate the stiffness values in Table I, is shown for each prototype by a solid line. The gradient of the axial force correlates to the axial stiffness according to (1). The values of prototype A can be compared with those in Table I as the geometry is equal.

In a similar way, the torque and force coefficients and the radial stiffness were measured with prototypes A-P1 and B. For the bearing coefficient, the rotor was levitated at standstill with its rotational axis in horizontal position. Then, a weight was radially applied, and the bearing current was measured. The torque coefficient was measured also at standstill with a lever

TABLE III
MEASUREMENT RESULTS OF BEARING AND DRIVE PARAMETERS.
VALUES IN BRACKETS ARE SIMULATED

Prototype	A-P1	A-P2	B	
axial stiffness	8.1 (8.7)	12.2 (12.1)	17.4 (16.2)	N/mm
radial stiffness	-16.6 (-18) -8.0 (-10)	---	-27.6 (-27.2)	Nm/A
torque coefficient	0.144 (0.147)	---	0.188 (0.190)	Nm/A
force coefficient	2.97 (2.72)	---	4.34 (4.83)	N/A

that pulls on a force measurement device, whereas the drive current was measured. The radial stiffness can be measured by displacing the rotor and measuring the bearing current. As the bearing performance of prototype A-P2 is too bad to hold the rotor weight in horizontal position, these measurements were not possible with this motor. The results are shown in Table III. The values in brackets show the simulation results.

The axial stiffness measurement of two-pole-pair rotor P2 showed an increase of 50% compared with rotor P1 in prototype A. Due to the increased size, the stiffness of prototype B is even 43% higher than that of prototype A-P2.

The simulation results fit very well to the measurements of stiffness and force and drive constant. Therefore, not only the impact of the pole pair number on the stiffness is proven but also the correctness of the simulation used in the previous sections is confirmed.

C. Losses

Increasing the pole pair number significantly affects the losses of the machine as the frequencies of magnetic fields and currents are increased. In particular, the main losses of this type of bearingless machine, which are losses in the stator iron and eddy-current losses in the copper, are strongly frequency dependent, as demonstrated in [19] and [20].

When the pole pair number is increased from one to two, there are different effects influencing the losses. As most loss components quadratically depend on the frequency, these losses will be increased by a factor of four. Additionally, the field distribution of a two-pole-pair rotor might show higher spatial harmonics, which was already shown in Fig. 5. This increases these losses even more.

Additionally, there exist losses that do not depend on the magnetic field, for example, controller losses, air friction losses at the rotor surface [21], losses due to carrier harmonics [22]–[24], or resistive copper losses depending on the load torque.

The losses in the machines were measured with a digital oscilloscope by multiplying instantaneous current and voltage and subsequent averaging over time. In Fig. 12, the measured losses of the prototypes are plotted against the rotational speed. As the maximum copper losses are below 2 W in both motors, they are not explicitly illustrated.

It shows that the losses of prototype A-P2 are higher than those of prototype A-P1 by a factor of around 2.2 due to the increased pole pair number. Due to the increase in size, the losses of prototype B are additionally increased by a factor of 2.1. At the same circumferential speed, prototype A-P1 produces the lowest losses.

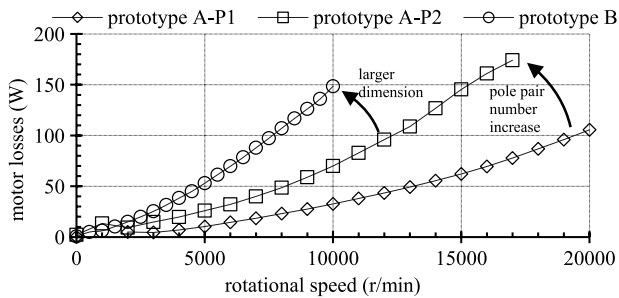


Fig. 12. Measured power consumption of the prototypes in no-load operation shown for different electrical frequencies.

Therefore, for high rotational speeds and high circumferential speeds, which is important for applications like pumps and blowers, a low pole pair number is preferable. In particular, the lower spatial harmonics in the rotor magnetization is a big advantage of the one-pole-pair rotor. However, there is still the possibility of reducing the losses of the two-pole-pair motor by improved magnetization and by using stranded litz wires and therefore omitting eddy current losses in the coils. This will be an issue of further research.

VI. CONCLUSION

Summarizing, it can be said that, at disk-type motors, a two-pole-pair rotor will lead to significantly higher and isotropic passive bearing stiffness values. A novel coil topology has been proposed, which is possible with a two-pole-pair rotor. A motor with 36 coils was built to demonstrate the feasibility of this two-pole-pair machine. It showed a very stable operational behavior with a small resonance range and high isotropic stiffness values.

However, it also showed that the losses of a two-pole-pair rotor are roughly twice as high as with a one-pole-pair rotor. Especially when high speeds are required, the one-pole-pair rotor is better due to its low losses. If the bearing stiffness is not sufficient for the required application, which can be the case in pumps and blowers, a two-pole-pair motor can be chosen.

REFERENCES

- [1] X. Sun, L. Chen, and Z. Yang, "Overview of bearingless permanent-magnet synchronous motors," *IEEE Trans. Ind. Electron.*, vol. 60, no. 12, pp. 5528–5538, Dec. 2013.
- [2] F. Zürcher, T. Nussbaumer, and J. W. Kolar, "Motor torque and magnetic levitation force generation in bearingless brushless multipole motors," *IEEE/ASME Trans. Mechatronics.*, vol. 17, no. 6, pp. 1088–1097, Dec. 2012.
- [3] J. Asama, D. Kanehara, T. Oiwa, and A. Chiba, "Development of a compact centrifugal pump with a two-axis actively positioned consequent-pole bearingless motor," *IEEE Trans. Ind. Appl.*, vol. 50, no. 1, pp. 288–295, Jan./Feb. 2014.
- [4] M. Ooshima and C. Takeuchi, "Magnetic suspension performance of a bearingless brushless DC motor for small liquid pumps," *IEEE Trans. Ind. Appl.*, vol. 47, no. 1, pp. 72–78, Jan./Feb. 2011.
- [5] B. Warberger, R. Kaelin, T. Nussbaumer, and J. W. Kolar, "50-Nm/2500-W bearingless motor for high-purity pharmaceutical mixing," *IEEE Trans. Ind. Electron.*, vol. 59, no. 5, pp. 2236–2247, May 2012.
- [6] T. Reichert, T. Nussbaumer, and J. W. Kolar, "Bearingless 300-W PMSM for bioreactor mixing," *IEEE Trans. Ind. Electron.*, vol. 59, no. 3, pp. 1376–1388, Mar. 2012.
- [7] S.-M. Yang and M.-S. Huang, "Design and implementation of a magnetically levitated single-axis controlled axial blood pump," *IEEE Trans. Ind. Electron.*, vol. 56, no. 6, pp. 2213–2219, Jun. 2009.

- [8] A. Kailasan, T. Dimond, P. Allaire, and D. Sheffler, "Design and analysis of a unique energy storage flywheel system—An integrated flywheel, motor/generator, and magnetic bearing configuration," *J. Eng. Gas Turbines Power*, vol. 137, no. 4, Apr. 2015, Art. ID. 042505.
- [9] S. Silber *et al.*, "High-speed drive for textile rotor spinning applications," *IEEE Trans. Ind. Electron.*, vol. 61, no. 6, pp. 2990–2997, Jun. 2014.
- [10] H. Mitterhofer, B. Mrak, and W. Amrhein, "Suitability investigation of a bearingless disk drive for micro turbine applications," in *Proc. IEEE ECCE*, 2013, pp. 2480–2485.
- [11] D. Steinert, T. Nussbaumer, and J. W. Kolar, "Slotless bearingless disk drive for high-speed and high-purity applications," *IEEE Trans. Ind. Electron.*, vol. 61, no. 11, pp. 5974–5986, Nov. 2014.
- [12] D. Steinert, T. Nussbaumer, and J. W. Kolar, "Concept of a 150 krpm bearingless slotless disc drive with combined windings," in *Proc. IEEE IEMDC*, Chicago, IL, USA, 2013, pp. 311–318.
- [13] H. Mitterhofer, W. Gruber, and W. Amrhein, "On the high speed capacity of bearingless drives," *IEEE Trans. Ind. Electron.*, vol. 61, no. 6, pp. 3119–3126, Jun. 2014.
- [14] S. Kobayashi, M. Ooshima, and M. N. Uddin, "A radial position control method of bearingless motor based on d-q-axis current control," *IEEE Trans. Ind. Appl.*, vol. 49, no. 4, pp. 1827–1835, Jul./Aug. 2013.
- [15] M. Ooshima, S. Kobayashi, and M. N. Uddin, "Magnetic levitation tests of a bearingless motor based on d-q axis current control," in *Conf. Rec. IEEE IAS Annu. Meeting.*, 2012, pp. 1–7.
- [16] H. Mitterhofer, W. Amrhein, and H. Grabner, "Comparison of two- and four-pole rotors for a high speed bearingless drive," presented at The 13th Int. Symp. Magnetic Bearings, ISMB, Arlington, VA, USA, 2012.
- [17] Y. Okada, "Self-bearing motors," in *Magnetic Bearings*, E. H. Maslen and G. Schweitzer, Eds. Berlin, Germany: Springer-Verlag, 2009, pp. 461–485.
- [18] D. Steinert, T. Nussbaumer, and J. W. Kolar, "Topology evaluation of slotless bearingless motors with toroidal windings," in *Proc. IPEC-Hiroshima-ECCE-ASIA*, 2014, pp. 975–981.
- [19] Y. Guo, J. G. Zhu, J. Zhong, H. Lu, and J. X. Jin, "Measurement and modeling of rotational core losses of soft magnetic materials used in electrical machines: A review," *IEEE Trans. Magn.*, vol. 44, no. 2, pp. 279–291, Feb. 2008.
- [20] S. Iwasaki *et al.*, "Influence of PWM on the proximity loss in permanent-magnet brushless AC machines," *IEEE Trans. Ind. Appl.*, vol. 45, no. 4, pp. 1359–1367, Jul./Aug. 2009.
- [21] M. S. Raymond, M. E. Kasarda, and P. E. Allaire, "Windage power loss modeling of a smooth rotor supported by homopolar active magnetic bearings," *J. Tribol.*, vol. 130, no. 2, Mar. 2008, Art. ID. 021101.
- [22] K. Yamazaki and A. Abe, "Loss investigation of interior permanent-magnet motors considering carrier harmonics and magnet eddy currents," *IEEE Trans. Ind. Appl.*, vol. 45, no. 2, pp. 659–665, Mar./Apr. 2009.
- [23] M. van der Geest, H. Polinder, and J. A. Ferreira, "Influence of PWM switching frequency on the losses in PM machines," in *Proc. IEEE ICEM*, 2014, pp. 1243–1247.
- [24] K. Yamazaki, T. Fukuoka, K. Akatsu, N. Nakao, and A. Ruderman, "Investigation of locked rotor test for estimation of magnet PWM carrier eddy current loss in synchronous machines," *IEEE Trans. Magn.*, vol. 48, no. 11, pp. 3327–3330, Nov. 2012.



Daniel Steinert (S'13) was born in Roth, Germany, in 1987. He received the M.Sc. degree in mechatronics from Dresden University of Technology, Dresden, Germany, in 2012, where he focused on micromechatronics and precision engineering. Since 2012, he has been working toward the Ph.D. degree at the Power Electronic Systems Laboratory, Swiss Federal Institute of Technology Zurich (ETH Zurich), Zurich, Switzerland, where he works on high-speed bearingless motors.

His current research is focused on bearingless motor topologies, control concepts, losses, and applications of bearingless motors.



Thomas Nussbaumer (S'02–M'06) was born in Vienna, Austria, in 1975. He received the M.Sc. (Hons.) degree in electrical engineering from Vienna University of Technology, Vienna, in 2001 and the Ph.D. degree from the Swiss Federal Institute of Technology Zurich (ETH Zurich), Zurich, Switzerland, in 2004.

From 2001 to 2006, he was with the Power Electronic Systems Laboratory, ETH Zurich, where he was involved in research on modeling, design, and control of three-phase rectifiers, power factor correction techniques, and electromagnetic compatibility. Since 2006, he has been with Levitronix GmbH, Zurich, where he is currently involved in research on bearingless motors, magnetic levitation, and permanent-magnet motor drives for the semiconductor and biotechnology industry. His current research is focused on compact and high-performance mechatronic systems, including novel power electronics topologies, control techniques, drive systems, sensor technologies, electromagnetic interference, and thermal aspects.



Johann W. Kolar (S'89–M'91–SM'04–F'10) received the M.Sc. and Ph.D. degrees (*summa cum laude*) from Vienna University of Technology, Vienna, Austria.

He is currently a Full Professor with and the Head of the Power Electronic Systems Laboratory, Swiss Federal Institute of Technology Zurich (ETH Zurich), Zurich, Switzerland. He has proposed numerous novel pulsewidth-modulation converter topologies and modulation and control concepts, published more than 650 scientific papers in international journals and conference proceedings, and filed more than 110 patents. The focus of his current research is on ultracompact and ultraefficient converter topologies employing latest power semiconductor technology (SiC and GaN), wireless power transfer, solid-state transformers, power supplies on chip, and ultrahigh-speed and bearingless motors.

Prof. Kolar was a recipient of 21 IEEE TRANSACTIONS and conference prize paper awards, the 2014 SEMIKRON Innovation Award, the 2014 IEEE Power Electronics Society R. David Middlebrook Award, and the ETH Zurich Golden Owl Award for Excellence in Teaching.